Optimizing turbulent inflow conditions for large-eddy simulations of the atmospheric boundary layer

Giacomo Lamberti[a,*], Clara García-Sánchez[b], Jorge Sousa[a], Catherine Gorlé[a]

[a] *Stanford University, Y2E2 Building, 473 Via Ortega, Stanford, CA, 94305*
[b] *Carnegie Institution for Science, 260 Panama St, Stanford, CA, 94305*

Abstract

Large-eddy simulations (LES) of the atmospheric boundary layer (ABL) require the specification of a turbulent inflow condition with appropriate turbulence intensities and length scales. When using a synthetic turbulence generator, the statistics obtained downstream of the inlet might deviate considerably from the intended values. In the present work we propose a fully automated approach to modify the input parameters for the turbulence generator such that the desired turbulence statistics are obtained at the downstream location of interest. The method employs a gradient-based optimization in combination with the divergence-free version of the digital filter method developed by Xie and Castro [1, 2]. A sensitivity analysis showed that the spanwise and vertical Reynolds stresses and length scales are the most influential input parameters. Hence, the optimization adjusts these parameters until the desired turbulence statistics are obtained downstream in the domain. The results demonstrate the promising capabilities of the method: the mean velocity profile is correctly maintained using an appropriate wall function, while the optimization results in Reynolds stresses, integral length-scales and turbulence spectra that compare well to ABL wind tunnel measurements.

Keywords: large-eddy simulations, atmospheric boundary layer, synthetic turbulence generator, gradient-based optimization

*Corresponding author
Email addresses: giacomol@stanford.edu (Giacomo Lamberti), gsclara@stanford.edu (Clara García-Sánchez), jsousa@stanford.edu (Jorge Sousa), gorle@stanford.edu (Catherine Gorlé)

1. Introduction

Computational fluid-dynamics (CFD) is increasingly employed in the wind engineering practice, and could, for example, represent a powerful tool for estimating mean and peak pressure distributions on buildings. An important challenge is that atmospheric boundary layer (ABL) simulations are influenced by uncertainties in the inflow boundary conditions and the turbulence model, which can strongly impact the accuracy of the results. For Reynolds-averaged Navier-Stokes (RANS) simulations, both these types of uncertainties have been shown to significantly affect the results [3, 4]. When using well-resolved large-eddy simulations (LES), which solve the filtered Navier-Stokes equations and only require a model for the subgrid-scale turbulence, the uncertainty related to the turbulence model can be reduced. However, the influence of the inflow boundary conditions is not eliminated. The remaining challenge is the definition of a turbulent inflow boundary condition that accurately represents the ABL flow in terms of the mean velocity, the turbulence intensities, and the turbulence length scales.

The methods to generate a turbulent inflow condition are generally classified in two categories: precursor methods and synthetic turbulence generators. Precursor or recycling methods employ either a separate simulation or a region upstream of the domain of interest to generate the turbulent inflow condition [5–11]. These methods resolve upstream roughness elements in the simulations to generate turbulence characteristic of an ABL. The computational cost of this approach presents a limitation for practical wind engineering applications. Moreover, the resulting boundary layer characteristics will depend on the chosen roughness configuration, providing only indirect control over the turbulence statistics. When the initial configuration does not provide the desired Reynolds stresses and integral length-scales, a time-consuming trial and error approach that involves modifying the roughness configuration and re-meshing the domain is required. Sensitivity or uncertainty quantification (UQ) studies to assess the influence of the inflow turbulence characteristics on the solution would require

repeating this procedure for each inflow condition of interest.

Synthetic turbulence generators represent an efficient alternative, providing full control over the turbulence statistics near the inflow boundary at a lower computational cost. They can be further classified as digital filter methods, random field generation (RFG) methods, or synthetic eddy methods (SEM), which each have their strengths and weaknesses. Several variants of digital filter methods, which produce coherent structures in space and time by filtering a random velocity field, were specifically developed for ABL applications [1, 2, 9–12]. Their main limitation is that they do not automatically generate a divergence-free velocity field; corrections need to be applied to avoid spurious pressure fluctuations in the domain [2]. The RFG methods generate a turbulent flow field that is guaranteed to be divergence-free, but their drawback is that the resulting velocity field is characterized by Gaussian spectra and therefore not representative of an ABL [10, 13]. As a result, modifications to provide desired turbulence spectra and correlations are required [14, 15]. The SEM methods, which produce velocity fluctuations based on the superposition of eddies [9, 11, 16–19], also do not guarantee a divergence-free velocity field. Finally, an important shared limitation of all digital filter methods is that the generated turbulent velocity field is not a solution of the system of equations being solved. As a result, the specified inflow statistics will develop towards an equilibrium condition downstream of the inlet, and the final result will depend on the subgrid model, the wall model, and the discretization used. It is not uncommon to observe a strong decrease in the turbulence intensity between the inlet and the downstream location of interest [20, 21]. The problem is similar to the horizontal inhomogeneity observed in RANS simulations of the ABL [22, 23], but the solution is more involved because of the complex interaction between the wall model, the subgrid model, and the numerics. For example, modifications to the wall function can improve the performance in terms of the mean velocity profile, but the decay in the turbulence intensity remains.

The objective of this study is to develop a method that efficiently overcomes this problem and enables simulations of wind loading on buildings in a variety

of turbulent ABL conditions. We employ the divergence-free turbulent inflow condition developed by Xie and Castro [2], which uses the mean velocity profile, Reynolds stress profiles and turbulence length scales as input parameters. This boundary condition is combined with a gradient-based optimization algorithm to find the values for these input parameters that result in the desired turbulence statistics at our downstream location of interest. The approach was designed to not require the representation of any upstream roughness elements, such that the target ABL characteristics can be achieved with minimal user intervention.

The method is tested on an experiment performed in the ABL wind tunnel of the Polytechnic University of Milan [24]. We perform simulations of this neutral wind tunnel ABL, using the grid resolution, wall model, and subgrid model that will be employed in future simulations of a high-rise building. A baseline simulation, using the target turbulence statistics as input parameters, is used to demonstrate the turbulence decay. Subsequently, a sensitivity analysis is performed to inform the formulation of the objective function for the optimization algorithm. Finally, the performance of the optimization algorithm is tested, comparing the final results to the experimental data in terms of the mean velocity, Reynolds stress and length scale profiles, and in terms of power spectral densities.

In the following, the wind tunnel experiment used for validation is summarized first. In section 3, the LES set-up is presented, and section 4 presents the baseline simulation results and sensitivity analysis. In section 5 the formulation of the objective function and the results of the optimization are discussed. Conclusions and plans for future work are presented in section 7.

2. Wind tunnel experiment

The ABL facility of the Polytechnic University of Milan is a closed circuit wind tunnel with a 35m long, 14m wide and 4m high test section. Spires and roughness elements are situated upstream in the test section to generate the desired neutral ABL (Figure 1 on the left). The models are placed at a distance of 10m from the inlet, in the center of a turntable of radius 6.5m, to enable tests

for different wind directions. Several tests were performed with the roughness configuration shown in Figure 1. First, the ABL in absence of a building model was characterized on a plane normal to the ABL mean flow direction at the center of the turntable using 3D hot-wire measurements with a sampling frequency of 2000Hz [25]. Subsequently, several experiments to measure the wind pressure on a high-rise building model were performed [25].

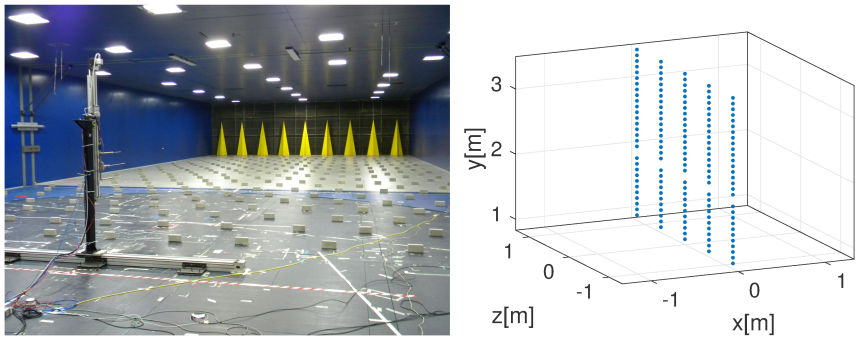

Figure 1: Experimental setup of the ABL wind tunnel of the Polytechnic University of Milan (left); coordinates of the 280 measurement points on a spanwise-vertical plane at the center of the turntable (right).

In the present work we focus on the experiment performed without the model to test the capabilities of our inflow generation framework. The experimental data consists of 20 second time-series of the three components of velocity at 280 points distributed on a plane in the middle of the turntable. The spanwise resolution of the measurements is 0.6m, while the vertical one is 43.7mm below 0.75m and 87.5mm above (Figure 1 on the right). The resulting mean velocity profiles obtained at five spanwise locations are shown in Figure 2 (top-left). On average, they represent a neutral ABL log law with a friction velocity $u_\star$ of 0.49m/s and a roughness height z_0 of 3.2mm. The corresponding profiles for the streamwise Reynolds stress component $\overline{u'^2}$ and the streamwise turbulence length-scale ${}^{x}L_u$, are shown in Figure 2 (top-right and bottom).

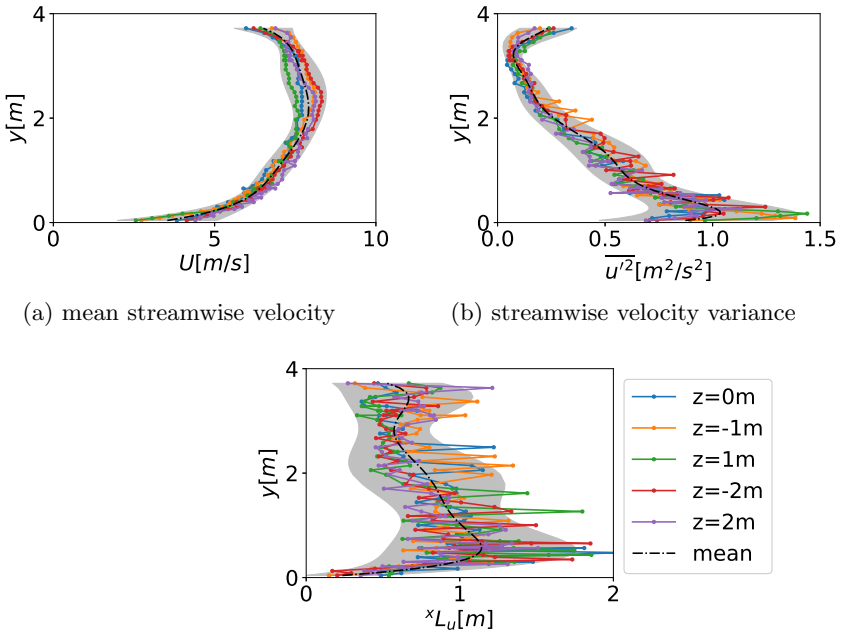

(a) mean streamwise velocity

(b) streamwise velocity variance

(c) streamwise length-scale

Figure 2: Spanwise-averaged (dash-dotted line) and spanwise variation (gray region) of the wind tunnel ABL measurements.

The plots show a spanwise variability in the profiles. Throughout the remainder of this paper, a polynomial fit to the average of the spanwise profiles is plotted using a dash-dotted line; the spanwise variability is represented using a gray shaded region defined by polynomial fits to the minimum and maximum values measured. The gray region will be used as the target region for the simulation results. Profiles for the other Reynolds stress components and length scales showed similar variability and are presented in the following sections for comparison to the data. In addition, velocity spectra will be used for comparison with the simulation results.

3. LES set-up

We use the pisoFOAM solver of OpenFOAM v4.0 to solve the filtered incompressible Navier-Stokes equations for a neutral ABL flow with the standard

Smagorinsky model ($C_s = 0.17$). All the simulations are performed using the Extreme Science and Engineering Discovery Environment (XSEDE) resources [26]. The following sections describe the computational domain and mesh, the boundary conditions, and the discretization and solution procedure.

3.1. Computational domain and mesh

The computational domain is 10m in the streamwise direction (x), 4m in the vertical direction (y) and 3m in the spanwise direction (z). It is smaller than the actual wind tunnel to limit the computational cost, but sufficiently large to achieve our objective of testing the inflow boundary condition. The mesh counts $\sim$5 million hexahedral cells, which includes refinements near the ground wall, where the minimum cell resolution is 12.5mm in the horizontal and 6.25mm in the vertical, resulting in a mean y^+ of $\sim$100.

3.2. Boundary conditions

The upper wall of the wind tunnel is not included in the simulations; instead we impose a slip boundary condition at the top. At the lower wall, a rough-wall logarithmic wall function is employed. The formulation is similar to the wall function commonly used in RANS simulations of the ABL [23, 27], but it is applied to the instantaneous flow field [28, 29]; it is designed to guarantee horizontal homogeneity of the ABL mean velocity profile.

The left and right boundaries are periodic, and the outlet is a pressure-outlet. At the inlet we impose the logarithmic mean velocity profile from the experiment. Synthetic turbulence is inserted just downstream of the inlet at the inflow generation plane, using the digital filter method developed by Xie and Castro [1, 2]. By imposing the turbulent velocity field on a plane inside the domain, it passes through the PISO (Pressure Implicit with Splitting of Operator) algorithm, and is adjusted to become divergence-free [2]. This eliminates non-physical pressure fluctuations that would otherwise be observed, which is especially important when estimating peak pressure loads on buildings. Figure 3 shows the location of the plane inside the domain, together with iso-surfaces

of the second invariant of the velocity gradient tensor Q [30], colored by values of velocity magnitude.

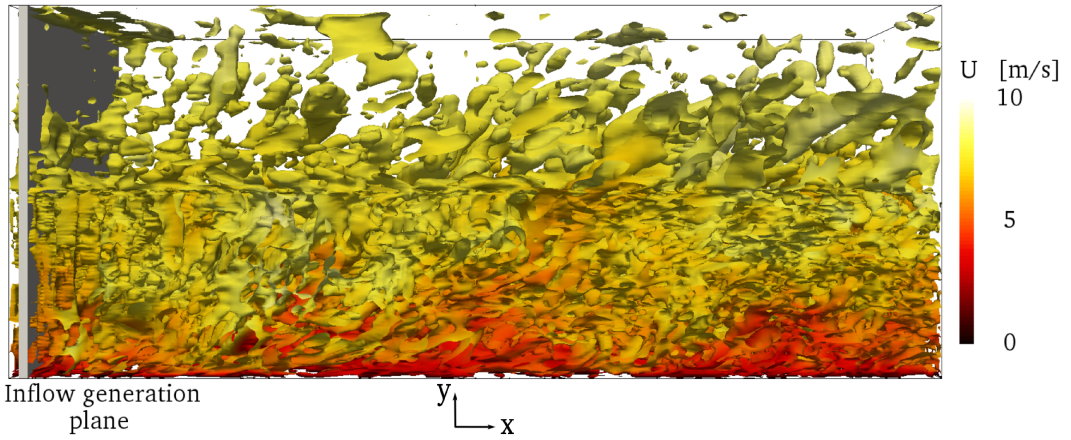

Figure 3: Generation of synthetic turbulence in the LES. Iso-surfaces of the second invariant of the velocity gradient tensor Q colored by values of velocity magnitude.

The turbulent velocity field imposed by the digital filter method is defined as follows:

$$u_i = U_i + a_{ij} u_{*,j}, \tag{1}$$

where U_i is the mean velocity, a_{ij} the Cholesky decomposition of the Reynolds stress tensor and $u_{*,j}$ is a fluctuation with a zero-mean and an exponential spatial and temporal correlation. The matrix a_{ij} is a function of the specified Reynolds stress profiles as a function of height; since the flow is homogeneous in the spanwise direction, the relevant Reynolds stress components are the normal stresses ($\overline{u'^2}$, $\overline{v'^2}$ and $\overline{w'^2}$), and the streamwise-vertical shear stress ($\overline{u'v'}$). The fluctuation $u_{*,j}$ is the filtered random field, which introduces the coherent structures. It requires the specification of the integral length scales, which are assumed to be constant with height, and are thus obtained from averaging the experimental values along the height.

Since the spatial resolution of the hot-wire measurements is insufficient to compute 2-point correlations, we rely on Taylor's hypothesis [31] to compute

the streamwise integral length-scales:

$$ {}^{x}L_u = UT_u, \quad {}^{x}L_v = UT_v, \quad {}^{x}L_w = UT_w, \tag{2} $$

where U is the streamwise component of the mean velocity and T_u, T_v and T_w are the integral time-scales. We then approximate the vertical and spanwise length-scales as follows [24]:

$$ {}^{y}L_u = 0.2{}^{x}L_u \; = \; {}^{y}L_v \; = \; {}^{y}L_w \tag{3} $$

$$ {}^{z}L_u = 0.3{}^{x}L_u \; = \; {}^{z}L_v \; = \; {}^{z}L_w \tag{4} $$

In summary, the turbulent velocity field of Equation 1 will be a function of the mean logarithmic velocity profile, four Reynolds stress profiles and three averaged time-scales.

3.3. Discretization and solution procedure

We differentiate the momentum equation using a central scheme and integrate in time using a backward Euler method with a time step of ∼0.002s. The resulting mean Courant number is less than 0.2, while the maximum varies between 1 and 2 throughout the simulation. In the baseline simulation of Section 4 we averaged statistics over a period of more than $40t_\star$ after an initialization period of $12.5t_\star$, where $t_\star = \delta/u_\star$ and δ is half of the domain height [2]. Subsequent simulations were initialized from the baseline result to accelerate the convergence, but the initialization period of $12.5t_\star$ was maintained. The simulations are stopped when the maximum difference in the Reynolds stresses calculated at a $\sim 4t_\star$ interval is less than 3%. The resulting simulated time is between 150-200s.

4. Baseline simulation results and sensitivity analysis

4.1. Streamwise inhomogeneity in the baseline simulation

We first performed a simulation imposing the desired mean velocity profile and turbulence statistics as inflow parameters, to verify the streamwise evolution of the flow statistics. All the profiles shown represent the variation over height

of the statistics of interest 5m downstream of the inlet at the mid spanwise location. Figure 4 shows that the mean velocity profile is maintained throughout the domain. This is a result of the formulation of the rough-wall logarithmic wall function, which is consistent with the ABL mean velocity profile imposed at the inlet.

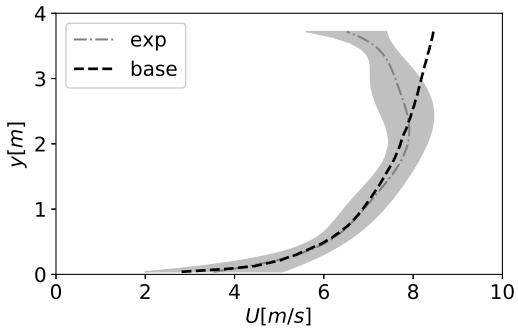

Figure 4: Comparison of the experimental mean velocity profile with the mean velocity profile computed by the baseline simulation 5m downstream of the inlet.

In contrast, Figure 5 shows that 5m downstream of the inflow generation plane (i.e. at the intended location of the building model in future LES) a decrease in turbulence kinetic energy of up to 50% is observed. This demonstrates the limitation of synthetic turbulence generators: since the imposed turbulent velocity field is not a solution of the system of equations being solved, the specified inflow statistics will develop towards an equilibrium condition that depends on the subgrid model, the wall model, and the discretization used.

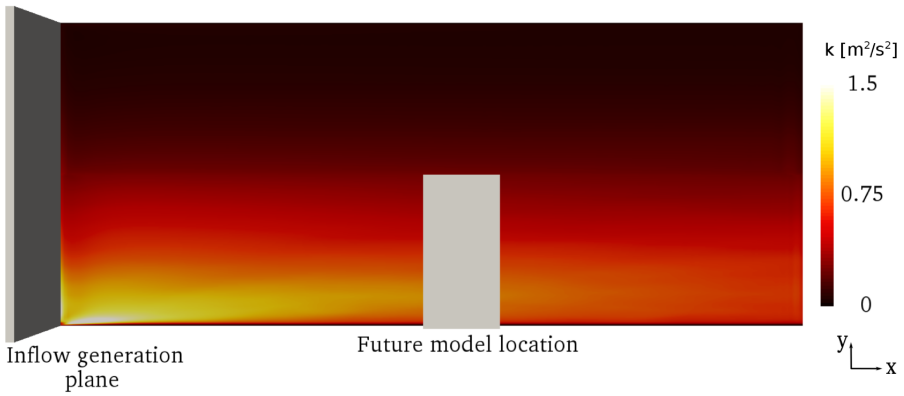

Figure 5: Decay of turbulence kinetic energy in the LES.

The turbulence decay can be seen in more detail in Figure 6, where the profiles of turbulence kinetic energy and Reynolds stresses 5m downstream of the inlet are compared with the spanwise-averaged wind tunnel profiles (i.e. the profiles imposed at the inflow). At 5m from the inlet, the streamwise velocity variance is up to ∼60% lower than the one imposed at the inflow and ∼50% lower on average. The vertical and spanwise components are decreased up to ∼60% and ∼50% respectively; the average decay is ∼45% for the vertical component and ∼20% for the spanwise component. We note that the Reynolds stresses plotted in Figure 6, and in the remainder of the paper, are the resolved stresses; the subgrid components are not considered because they are negligibly small.

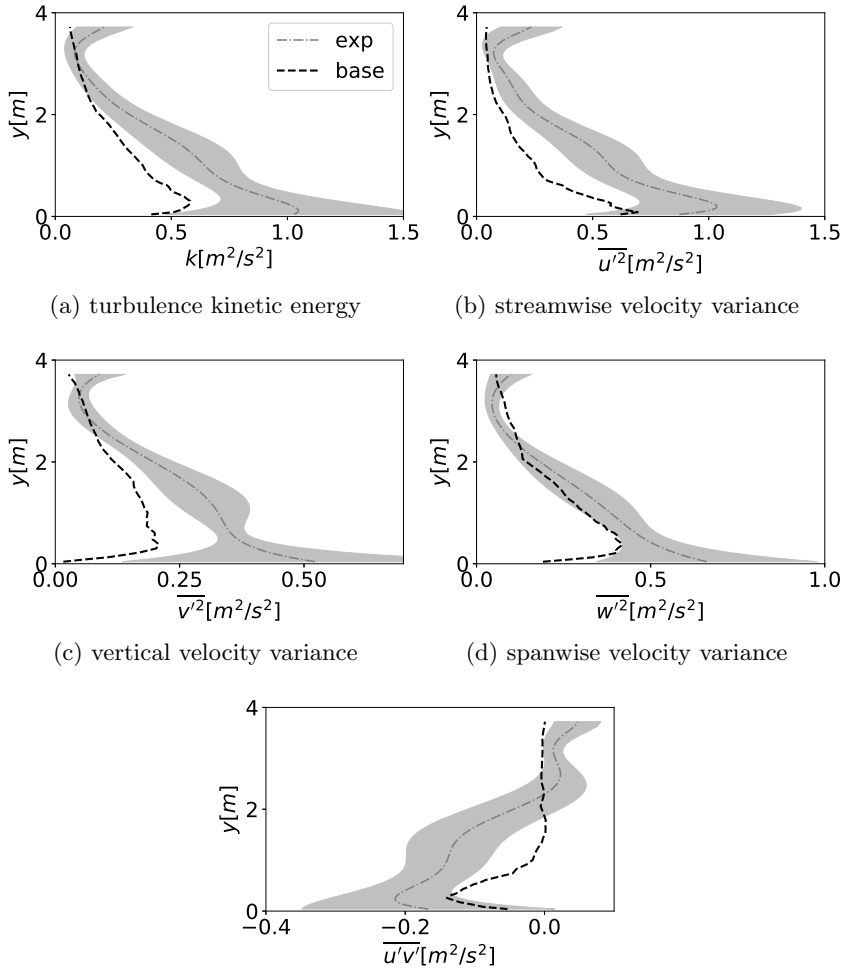

(a) turbulence kinetic energy

(b) streamwise velocity variance

(c) vertical velocity variance

(d) spanwise velocity variance

(e) streamwise-vertical shear stress

Figure 6: Comparison of the experimental turbulence kinetic energy and Reynolds stress profiles with the corresponding profiles computed by the baseline simulation 5m downstream of the inlet.

Figure 7 shows that the streamwise inhomogeneity in the integral length scales is smaller than that in the Reynolds stresses. The streamwise length scale modeled by the baseline LES is inside the gray target region up to 3m height, and quite close to the spanwise-averaged measurement. The vertical and spanwise components are overestimated, especially near to the ground. This is likely related to the fact that we specify a constant profile over height for the

turbulence length-scales at the inflow.

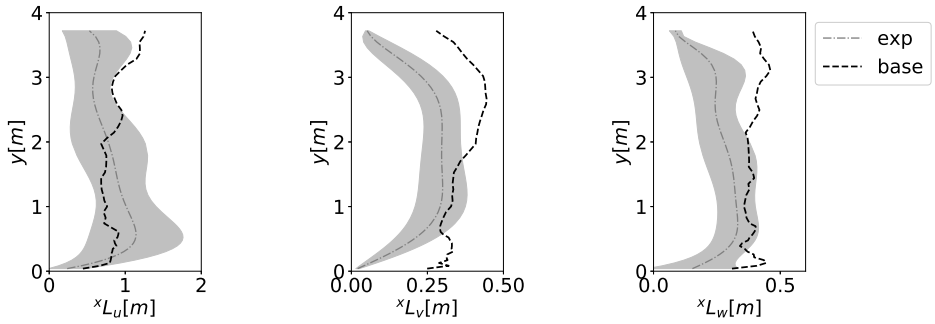

(a) streamwise length-scale (b) vertical length-scale (c) spanwise length-scale

Figure 7: Comparison of the experimental integral length scales with the length scales computed by the baseline simulation 5m downstream of the inlet.

4.2. Sensitivity analysis

To mitigate the effect of the observed turbulence decay on the quantities of interest, an optimization problem can be formulated to find the input parameters that will produce the desired turbulence statistics at the location of interest. To support the formulation of an effective objective function, we first performed a sensitivity analysis to identify the influence of the different input parameters on the quantities of interest.

The inflow algorithm is a function of the mean velocity profile, four Reynolds stress profiles and three integral time-scales. The baseline simulation confirmed that we can maintain the mean velocity profile by modifying the wall functions; hence, there is no need to change the logarithmic profile at the inflow generation plane. In addition, the shear stress $\overline{u'v'}$ will adjust automatically to changes in the normal components $\overline{u'^2}$ and $\overline{v'^2}$, following the realizability constraint $(\overline{u'v'})^2 \leq \overline{u'^2}\ \overline{v'^2}$ [32]. Based on these considerations, the input mean velocity and shear stress are not included in the sensitivity study. Hence, six additional LES simulations were performed, increasing the remaining parameters by a factor of two one at a time. For the Reynolds stresses this implies that the x-coordinate of the parametrization points of the Bezier curves was increased by a factor of

two (see Section 5.1).

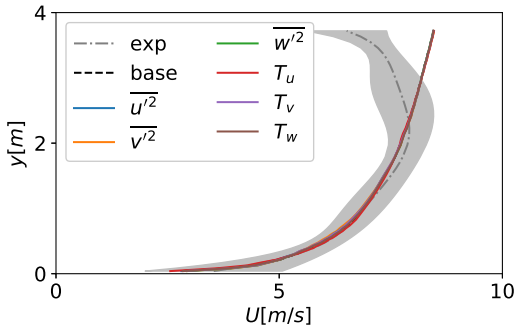

Figure 8: Influence of the inflow parameters on the mean velocity $5m$ downstream of the inlet. The inflow parameters are doubled one at a time; the legend indicates the doubled parameter.

Figure 8 shows the mean velocity profiles resulting from the six LES simulations compared to the baseline; the legend in the plot indicates which of the input parameters has been doubled. As expected, the profiles at the building location collapse to the baseline result: the only input parameter that matters for the mean velocity is the logarithmic inlet profile.

Figure 9 shows that the input parameters $\overline{u'^2}$, T_v and T_w have a relatively small effect on the turbulence kinetic energy and Reynolds stresses at the target location. Doubling the integral time-scale T_u at the inlet causes an even stronger turbulence decay than the one experienced by the baseline simulation, but when doubling the inflow $\overline{v'^2}$ and $\overline{w'^2}$, the resulting profile of the turbulence kinetic energy falls completely inside the target region. The influence of individual spanwise and vertical Reynolds stress components is stronger on their respective values further downstream, and they have a similar effect on $\overline{u'^2}$. In particular, when doubling $\overline{v'^2}$ at the inflow, the corresponding component at the building location is on average $\sim 60\%$ higher than the baseline result, while $\overline{u'^2}$ and $\overline{w'^2}$ experience an average increase of $\sim 40\%$ and $\sim 15\%$ respectively. When doubling $\overline{w'^2}$ at the inflow, the corresponding values at the downstream building location increase by $\sim 50\%$ on average compared to the baseline simulation. The resulting values exceed the target values, indicating that the imposed

perturbation might be too large. The streamwise and vertical Reynolds stress components also increase by $\sim 45\%$. As expected, the effect on the shear stress is similar to that on the streamwise and vertical velocity variance.

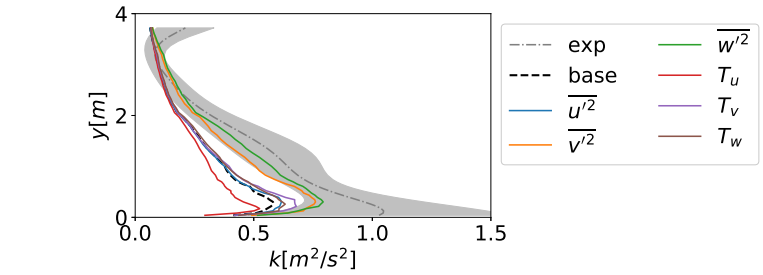

(a) turbulence kinetic energy

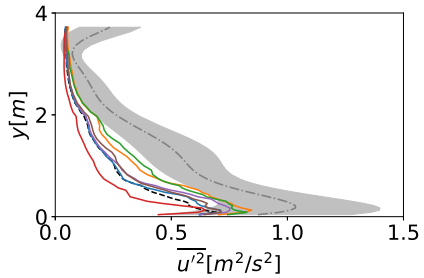

(b) streamwise velocity variance

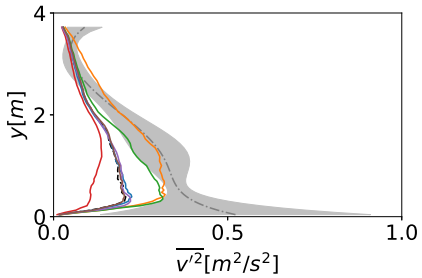

(c) vertical velocity variance

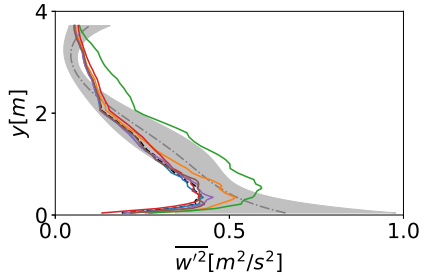

(d) spanwise velocity variance

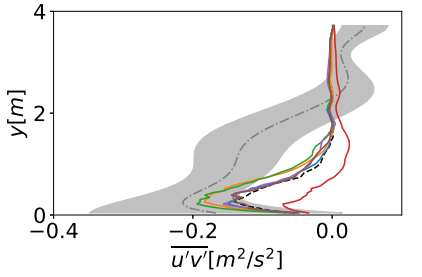

(e) streamwise-vertical shear stress

Figure 9: Influence of the inflow parameters on the Reynolds stresses $5m$ downstream of the inlet. The inflow parameters are doubled one at a time; the legend indicates the doubled parameter.

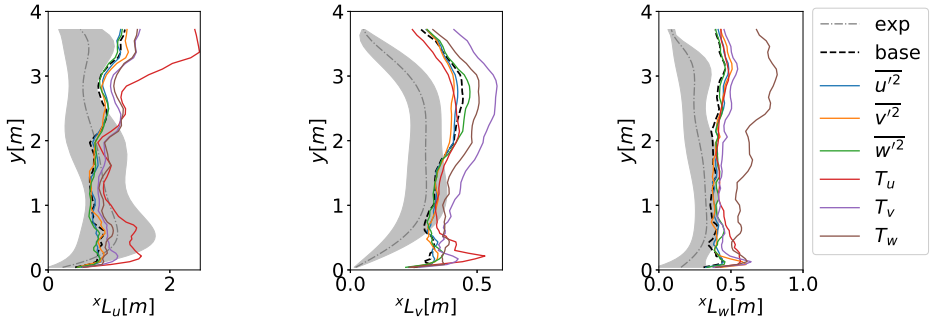

(a) streamwise length-scale (b) vertical length-scale (c) spanwise length-scale

Figure 10: Influence of the inflow parameters on the integral length scales $5m$ downstream of the inlet. The inflow parameters are doubled one at a time; the legend indicates the doubled parameter.

The downstream length-scale profiles are most sensitive to changes in their corresponding time- or length-scales at the inflow, as shown in Figure 10. The streamwise component increases by $\sim$50% on average when doubling T_u; increasing T_v causes a $\sim$28% mean increase in the vertical length-scale; doubling T_w produces an average $\sim$60% increase on the spanwise length-scale at the building. This trend is less consistent close to the wall, where the vertical length scale is more strongly affected by the streamwise value at the inlet, while the spanwise length scale is sensitive to both the streamwise and the vertical component.

The integral length-scales represent the size of the largest eddies, while the Reynolds stresses quantify the intensity of fluctuations. The result of the sensitivity analysis suggests an interaction between the Reynolds stresses and the turbulence length-scales. However, to perform the optimization, we modify the input Reynolds stresses that have a smaller influence on the target length-scales (i.e. $\overline{v'^2}$ and $\overline{w'^2}$), and the input length-scales that have a smaller effect on the target Reynolds stresses (i.e. T_v and T_w). These input variables thus support performing the optimization for the Reynolds stresses and the length scales independently.

5. Gradient-based optimization

We implemented a gradient-based optimization algorithm because the sensitivity analysis confirmed that the turbulence statistics change monotonically: higher Reynolds stresses or integral time scales at the inflow generation plane will result in higher Reynolds stresses or integral time scales at the future building location. The algorithm dynamically adjusts the input parameters of the synthetic turbulence generator, until the statistics at the location of interest are sufficiently close to the wind tunnel measurements. In the following we first describe the parameterization of the Reynolds stress profiles that will be used for the optimization. Subsequently we discuss the definition of the objective function.

5.1. Bezier parametrization

We parametrize the input Reynolds stresses using Bezier curves [33], to control the shape of the profiles throughout the optimization steps. A Bezier curve is defined by a number of control points; the curve passes through the first and last point, while it gets attracted by the intermediate points. Figure 11 shows the input Reynolds stresses $\overline{v'^2}$ and $\overline{w'^2}$ resulting from the parametrization with 8 control points; the control points are more concentrated in the region below $0.5m$, where the profiles experience the highest variation.

The optimization algorithm acts on the x-coordinate of the control points, except for the first and last one, which are fixed: the points are moved back and forth along the x-axis depending on the gradient of the objective function.

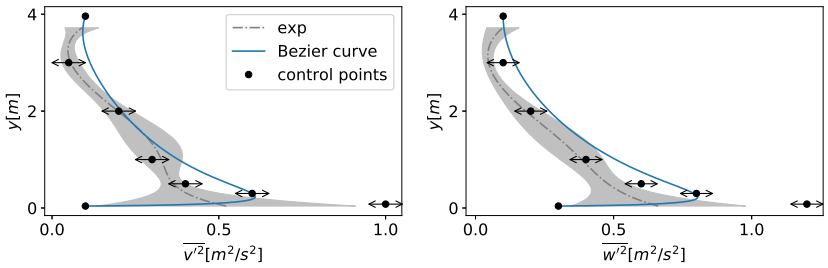

(a) vertical velocity variance (b) spanwise velocity variance

Figure 11: Parametrization of the input Reynolds stresses with Bezier curves.

5.2. Objective functions

The sensitivity study showed that the Reynolds stresses at the building can be increased by increasing $\overline{v'^2}$ and $\overline{w'^2}$ at the inflow. Therefore, we opt for a multi-objective optimization procedure, in which the decision variables are the profiles of $\overline{v'^2}$ and $\overline{w'^2}$ at the inflow generation plane. This should enable higher turbulence intensities at the downstream location, while maintaining integral length scales similar to the baseline result. Going one step further, we can also try to obtain better integral length scales by selecting the input T_v and T_w as additional decision variables. The input T_u was not included because it also affects the Reynolds stresses; we choose to separate the optimization of the integral length-scales from the optimization of the Reynolds stresses.

To solve the resulting multi-objective algorithm we rely on the scalarization technique, which is the simplest way of solving a multi-objective problem [34]. In the scalarization technique the objective functions are weighted and combined into a single objective function. The resulting function is a linear combination of the least-squares differences between the statistics obtained by the LES, and the corresponding target experimental values. Considering the Reynolds stresses as

our quantities of interest, the objective function assumes the following form:

$$
\begin{aligned}
f_p\Big((\overline{v'(y_p)^2})_i, (\overline{w'(y_p)^2})_i\Big) =& \frac{1}{2}\gamma_u\Big((\overline{u'(y_p)^2})_b - (\overline{u'(y_p)^2})_{exp}\Big)^2 \\
&+\frac{1}{2}\gamma_v\Big((\overline{v'(y_p)^2})_b - (\overline{v'(y_p)^2})_{exp}\Big)^2 \\
&+\frac{1}{2}\gamma_w\Big((\overline{w'(y_p)^2})_b - (\overline{w'(y_p)^2})_{exp}\Big)^2,
\end{aligned} \tag{5}
$$

where y_p is the height of the pth Bezier point, and γ_u, γ_v and γ_w are the weights. The subscripts $()_i$, $()_b$ and $()_{exp}$ indicate the Reynolds stresses at the inflow generation plane, at the future building location, or the target values from the experiment respectively. The weights need to sum to 1 and be strictly positive [34]; we chose them depending on the importance of each normal Reynolds stress relative to the turbulence kinetic energy, thus $\gamma_u = 0.5$, $\gamma_v = 0.2$ and $\gamma_w = 0.3$. We treat the 6 intermediate control points as independent; hence, we solve 6 optimization problems in parallel (i.e. one for each y_p value).

When we add the integral time-scales as quantities of interest, the objective function is completely analogous, but there is no vertical variation in this case:

$$
\begin{aligned}
f_T\Big(T_{v,i}, T_{w,i}\Big) = \frac{1}{2}\gamma_u\Big(T_{u,b} - T_{u,exp}\Big)^2 + \frac{1}{2}\gamma_v\Big(T_{v,b} - T_{v,exp}\Big)^2 \\
+\frac{1}{2}\gamma_w\Big(T_{w,b} - T_{w,exp}\Big)^2,
\end{aligned} \tag{6}
$$

where the weights are the same as before.

6. Results

In the following section we present the results of the two approaches described above, i.e. we solve two different optimization problems: one that minimizes the objective function of Equation 5 and another that minimizes both the objective functions of Equations 5 and 6.

6.1. Optimization of input Reynolds stresses

To compute the gradient from two non-trivial solutions at the start of the optimization, we employ the baseline result and perform an additional simulation doubling the input parameters that are decision variables, i.e. $\overline{v'^2}$ and $\overline{w'^2}$. We will refer to the baseline simulation as *step0* of the optimization and to the

additional simulation as *step1*. The input profiles of mean velocity, streamwise velocity variance and shear stress are obtained from the measurements and never modified by the code. The same holds for the input integral time-scales, which are specified as the average of the corresponding measurement over height. We ran one step of the optimization, which will be referred to as *step2*; the resulting input profiles for all three steps are plotted in Figure 12.

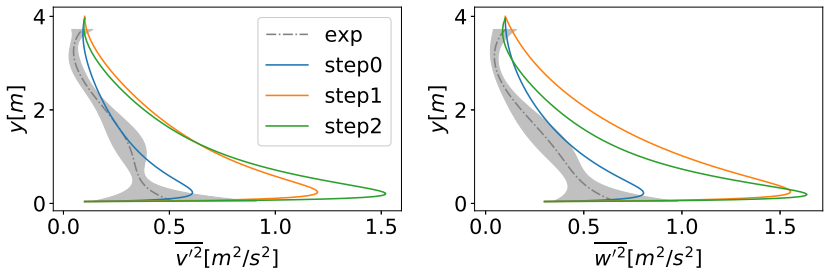

(a) vertical velocity variance (b) spanwise velocity variance

Figure 12: Input Reynolds stresses modified by the optimization.

The analysis of the results at the location of interest focuses on the Reynolds stresses and length scales; similarly to the sensitivity analysis, the mean velocity profile was not affected by the Reynolds stresses at the inflow.

Figure 13 shows the turbulence kinetic energy and Reynolds stresses at the future building location for the different steps. The results for *step0* are those from the baseline simulation. For *step1* the turbulence kinetic energy and Reynolds stresses $\overline{u'^2}$ and $\overline{v'^2}$ at the location of interest are already within the gray zone representing the spanwise variation of the measurements over most of the domain height. The values for $\overline{w'^2}$ become too high at the building location, the maximum discrepancy from the upper bound of the target region is $\sim 28\%$ and the average is $\sim 14\%$. This explains why in *step2*, the input profile of $\overline{v'^2}$ remains basically unchanged above $1m$ height, while $\overline{w'^2}$ is decreased to a value in between *step0* and *step1*. Near the ground, the optimization algorithm results in the strongest increase for both input Reynolds stresses, since the turbulence decay is stronger in this region.

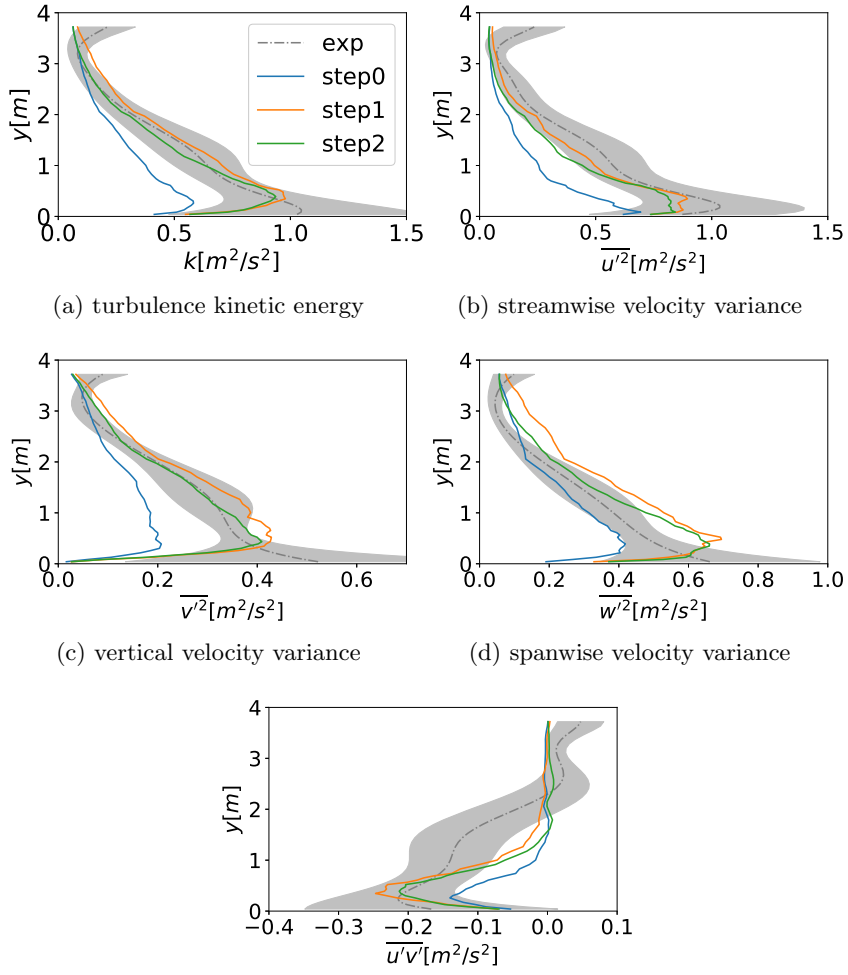

(a) turbulence kinetic energy

(b) streamwise velocity variance

(c) vertical velocity variance

(d) spanwise velocity variance

(e) streamwise-vertical shear stress

Figure 13: Reynolds stresses 5m downstream of the inlet as a result of the optimization.

The results show that only one step in the optimization is required to reach a level of turbulence kinetic energy at the building location that is very close to the spanwise-averaged profile of the experiment. $\overline{v'^2}$ is now entirely inside the gray region that represents the spanwise variation of the experiment, while $\overline{u'^2}$ satisfies the requirement below $1m$ and above $1.8m$. In the region in between, the discrepancy from the lower bound of the target region is $\sim 7\%$ on average. The wall-normal stress ($\overline{w'^2}$) remains slightly too high around $y = 0.5m$; here

the maximum discrepancy from the upper bound of the target region is $\sim 12\%$. The result for the shear stress is similar to that for the streamwise component: it falls inside the target region below $1m$ and above $1.8m$ height.

Figure 14 shows the effect of the optimization on the integral length scales. For the streamwise component the profile modeled by the simulation of *step2* is very close to the spanwise-averaged measurement below $y = 2.5m$, which is the region of interest for the future simulation with the high-rise building. Above this height the average deviation between the simulated profile and the upper bound of the gray region is $\sim 8\%$. The vertical component is within the gray region that represents the spanwise variation of the experiment between $y = 0.5m$ and $y = 2m$, but deviates more significantly close to the ground and above $2m$, where the average discrepancy is more than 50%. The spanwise integral length-scale is characterized by a similar behavior. The discrepancy close to the ground is most likely caused by the fact that the inflow generation algorithm requires specifying a constant value for the integral length-scales over height. As a result, the integral length-scales imposed near the ground at the inflow are larger than the length-scales obtained in the wind tunnel, and the optimization process can not compensate for this difference. For the vertical and spanwise length scales, the agreement with the measurement deteriorates between step 1 and step 2, which motivates including the length scales in the objective function for the optimization.

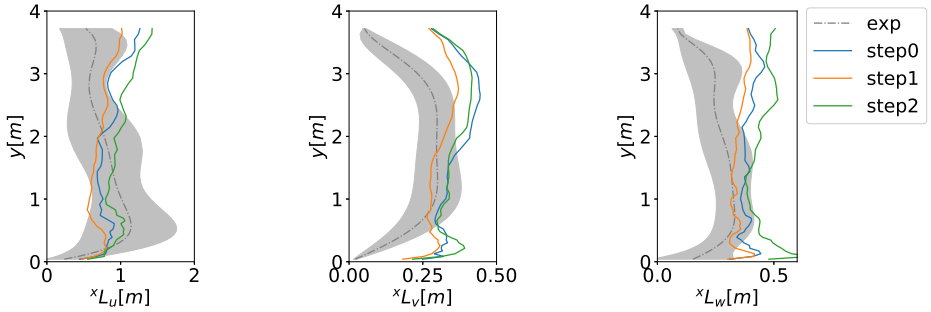

(a) streamwise length-scale (b) vertical length-scale (c) spanwise length-scale

Figure 14: Modeled integral length-scales 5m downstream of the inlet as a result of the optimization.

Figures 15 presents the spectra of the three velocity components at the downstream location of interest at $1m$ and $2m$ height. At both heights, the highest frequency captured by the hot-wires is $1000Hz$, while the LES resolves scales below $50Hz$, as evident from the energy decay above this frequency. In the range of resolved scales, the LES spectra agree well with the experiment, and the turbulence is resolved into the inertial sub-range. The optimization process is shown to improve the energy content in the LES, in particular in the inertial sub-range. The observations for the large-scale portion of the spectra are consistent with the results for the Reynolds stresses: the power spectrum of the spanwise velocity fluctuations reaches a higher energy content compared to the experiment, while the streamwise and vertical components are slightly underestimated.

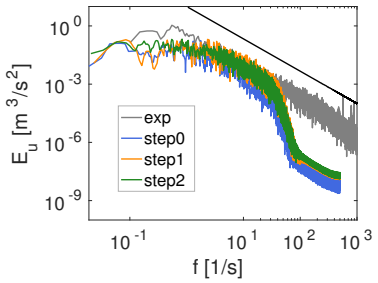

(a) streamwise velocity spectrum at $1m$ height

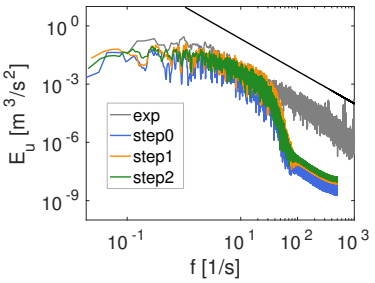

(b) streamwise velocity spectrum at $2m$ height

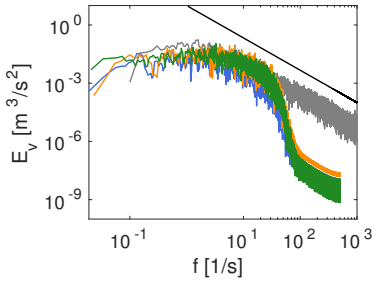

(c) vertical velocity spectrum at $1m$ height

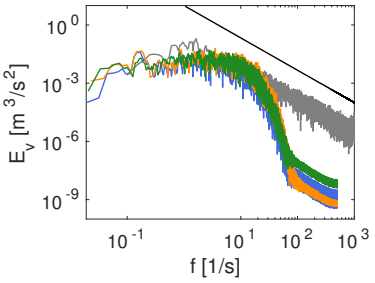

(d) vertical velocity spectrum at $2m$ height

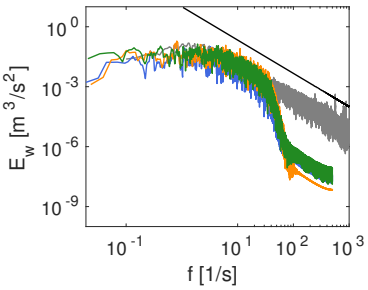

(e) spanwise velocity spectrum at $1m$ height

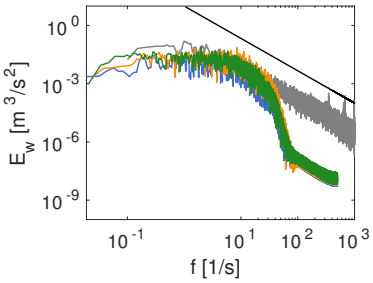

(f) spanwise velocity spectrum at $2m$ height

Figure 15: Modeled power spectrum, $5m$ downstream of the inlet, as a result of the optimization.

6.2. Optimization of input Reynolds stresses and time scales

When solving the optimization problem that minimizes both the objective functions of Equations 5 and 6, the input Reynolds stresses of the optimization step are exactly the same as before, while the input time scales are different. In this case we relied on the results of the sensitivity analysis to compute the

gradients of the integral time scales; by combining the information from the baseline and the two simulations in which we doubled T_v or T_w we can compute the new input integral time-scales using Equation 6.

Figure 16 compares the results of the two optimization problems for the Reynolds stresses, showing that the results are very similar. This is as expected, since the sensitivity analysis showed a small influence of the parameters T_v or T_w on the Reynolds stresses.

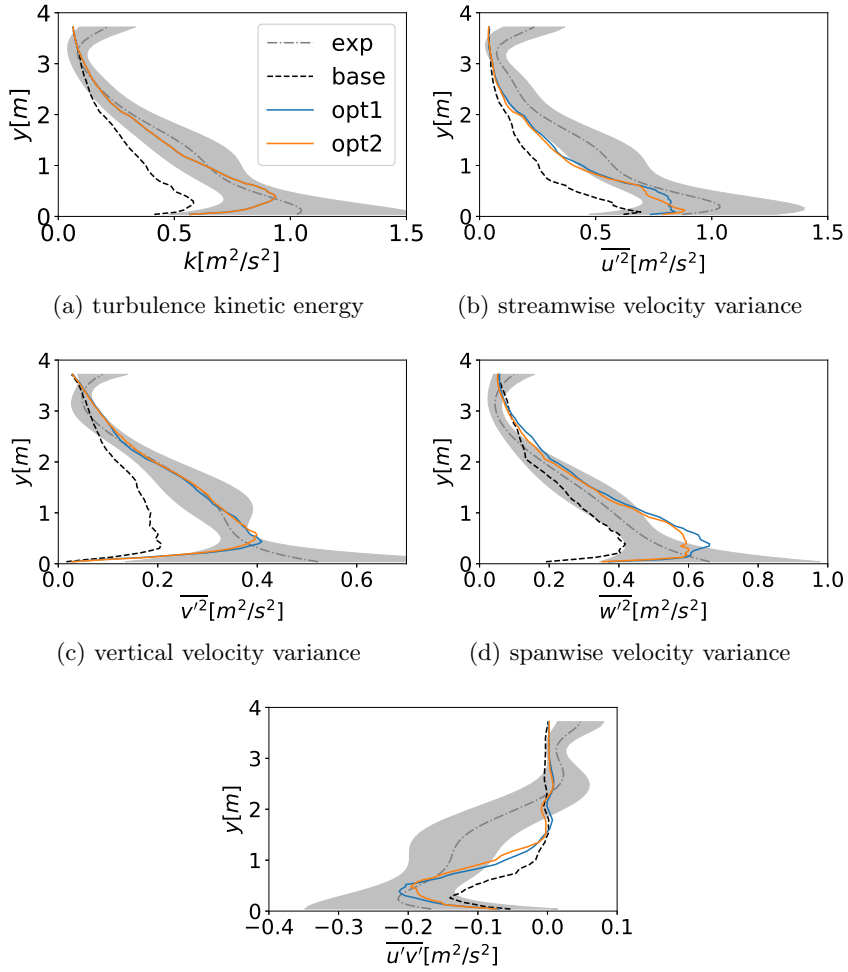

(a) turbulence kinetic energy

(b) streamwise velocity variance

(c) vertical velocity variance

(d) spanwise velocity variance

(e) streamwise-vertical shear stress

Figure 16: Modeled Reynolds stresses 5m downstream of the inlet as a result of the second optimization problem.

Figure 17 presents the turbulence length-scales at the building location, showing that the second optimization problem performs slightly better. The streamwise length scale is improved on the top part of the domain: it is outside the gray region just above $3m$ and the error is very small. The spanwise length-scale is closer to the spanwise-averaged measurement and almost everywhere inside the target region. The vertical component of the integral length

scale is very similar, but shows a slight improvement close to the wall. The results demonstrate that including the length scales in the objective function can improve the comparison with the experimental data. However, the fact that the input value for the length scale is constant with height limits the control in terms of reproducing the shape of the profile obtained from the experiment.

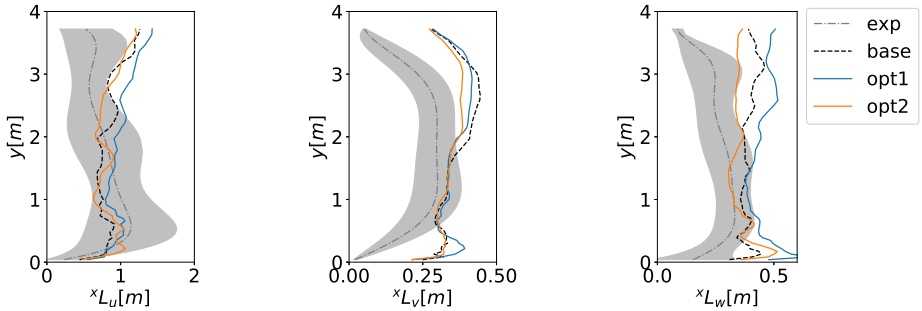

(a) streamwise length-scale (b) vertical length-scale (c) spanwise length-scale

Figure 17: Modeled integral length-scales 5m downstream of the inlet as a result of the second optimization problem.

7. Conclusions and future work

The definition of an appropriate turbulent inflow condition is essential when performing large-eddy simulations of surface layer phenomena. Digital filter methods can efficiently generate a representative velocity field with structures that are coherent in space and time, but their drawback is that this velocity field is not a solution of the system of equations being solved. As a result, the specified inlet ABL evolves throughout the domain, often resulting in too low turbulence intensities at downstream locations of interest. The objective of this study was to develop an efficient method to overcome this problem and enable LES of surface layer wind phenomena with a variety of incoming turbulence characteristics.

The proposed framework is formulated to obtain user-specified Reynolds stresses and turbulence length scales at a downstream location of interest in the computational domain; it does not attempt to solve the complex problem

of horizontal homogeneity that affects LES of ABL flows. The method is based on the divergence-free inflow condition developed by Xie and Castro [2], and incorporates a gradient-based optimization procedure to determine the input parameters that will result in the desired turbulence statistics at the location of interest. The method has been tested on simulations of a boundary layer generated in the ABL wind tunnel of the Polytechnic University of Milan. The location of interest was defined 5m downstream of the inlet, which corresponds to the location of a high-rise building model in future LES studies.

First, a sensitivity analysis was performed to identify the most influential parameters in the synthetic turbulence generator. In terms of the Reynolds stresses, the inlet values for $\overline{v'^2}$ and $\overline{w'^2}$ were found to have a significant effect on the turbulence intensities at the downstream location of interest. In terms of the length scales, the sensitivity analysis showed a dominant influence of the inlet values for T_v and T_w on the target integral length scales. Subsequently, this information was used to implement and test two different optimization approaches.

The first approach solves a multi-objective optimization algorithm that adjusts the inlet values for $\overline{v'^2}$ and $\overline{w'^2}$ to obtain the target Reynolds stresses at the downstream location of interest. The results show that the mean velocity profile downstream of the inflow is not affected by the change in the input Reynolds stresses and turbulence length scales. This is a result of the formulation of the rough-wall logarithmic wall function, which is consistent with the ABL mean velocity profile imposed at the inlet. For the Reynolds stress profiles the optimized result compares considerably better to the measurements than the baseline simulation. After one step in the optimization a maximum discrepancy of $\sim 12\%$ is found in the spanwise Reynolds stress component near 0.5m height. The effect of the input $\overline{u'^2}$ and $\overline{v'^2}$ on the integral length-scales is relatively small, but the agreement with the experimental data does deteriorate after one step of the optimization.

The second approach was implemented to overcome this problem: the optimization problem for the Reynolds stresses is identical as before, but an ad-

ditional objective function is incorporated to obtain the target length scales at the downstream location of interest by adjusting the input values for T_v and T_w. The results show an improvement in the predicted turbulence scales at the building location, but the vertical and spanwise length scales continue to be over predicted below 0.5m height. This is likely related to the fact that the input for the inflow length scale is a constant value over the height of the ABL, thereby not allowing to reproduce the shape of the experimental profile.

In summary, the proposed method provides an efficient way to design a LES of the ABL that provides user-specified turbulence statistics at a downstream location of interest in the domain. Future improvements to the code will primarily focus on a more accurate representation of the length scales. One could implement different inlet zones over the height of the surface layer, each with their own length scale. This would enable optimizing the length scales at different heights, similar to the process for optimizing the Reynolds stress profiles. We will also perform additional steps in the optimization to verify if the solution can be further improved, and implement an automatic stopping criteria that balances computational cost and maximum allowed discrepancy to the target profiles. Finally, the method will be used to quantify the effect of the turbulence intensities and length scales at the building site on the prediction of mean and peak wind pressure distributions, and the LES results will be compared against wind tunnel experiments.

8. Acknowledgements

This material is based upon work supported by the National Science Foundation under Grant Number 1635137, and used the Extreme Science and Engineering Discovery Environment (XSEDE), which is supported by National Science Foundation grant number CI-1548562.

The authors would like to acknowledge Dr. Luca Amerio, Dr. Stefano Giappino, Dr. Paolo Schito and Prof. Alberto Zasso, who performed the wind tunnel experiment at the Polytechnic University of Milan and provided the data

for the numerical validation. We also thank Prof. Zheng-Tong Xie and Prof. Ian P. Castro for sharing the algorithm of the digital filter method.

[1] Z. T. Xie and I. P. Castro. Efficient generation of inflow conditions for large eddy simulation of street-scale flows. *Flow, turbulence and combustion*, 81(3):449–470, 2008.

[2] Y. Kim, I. P. Castro, and Z. T. Xie. Divergence-free turbulence inflow conditions for large-eddy simulations with incompressible flow solvers. *Computers & Fluids*, 84:56–68, 2013.

[3] C. Gorlé, C. Garcia-Sanchez, and G. Iaccarino. Quantifying inflow and rans turbulence model form uncertainties for wind engineering flows. *Journal of Wind Engineering and Industrial Aerodynamics*, 144:202–212, 2015.

[4] C García-Sánchez, G Van Tendeloo, and C Gorlé. Quantifying inflow uncertainties in rans simulations of urban pollutant dispersion. *Atmospheric environment*, 161:263–273, 2017.

[5] T. S. Lund, X. Wu, and K. D. Squires. Generation of turbulent inflow data for spatially-developing boundary layer simulations. *Journal of Computational Physics*, 140(2):233–258, 1998.

[6] K. Nozawa and T. Tamura. Large eddy simulation of the flow around a low-rise building immersed in a rough-wall turbulent boundary layer. *Journal of Wind Engineering and Industrial Aerodynamics*, 90(10):1151–1162, 2002.

[7] K. Liu and R. H. Pletcher. Inflow conditions for the large eddy simulation of turbulent boundary layers: a dynamic recycling procedure. *Journal of Computational Physics*, 219(1):1–6, 2006.

[8] T. Tamura. Towards practical use of les in wind engineering. *Journal of Wind Engineering and Industrial Aerodynamics*, 96(10):1451–1471, 2008.

[9] G. R Tabor and M.H. Baba-Ahmadi. Inlet conditions for large eddy simulation: a review. *Computers & Fluids*, 39(4):553–567, 2010.

[10] A. K. Dagnew and G. T. Bitsuamlak. Computational evaluation of wind loads on a standard tall building using les. *Wind and Structures*, 18(5):567–598, 2014.

[11] X. Wu. Inflow turbulence generation methods. *Annual Review of Fluid Mechanics*, 49:23–49, 2017.

[12] S. J. Daniels, I. P. Castro, and Z.T. Xie. Peak loading and surface pressure fluctuations of a tall model building. *Journal of Wind Engineering and Industrial Aerodynamics*, 120:19–28, 2013.

[13] A Smirnov, S Shi, and I Celik. Random flow generation technique for large eddy simulations and particle-dynamics modeling. *Journal of Fluids Engineering*, 123(2):359–371, 2001.

[14] SH Huang, QS Li, and JR Wu. A general inflow turbulence generator for large eddy simulation. *Journal of Wind Engineering and Industrial Aerodynamics*, 98(10-11):600–617, 2010.

[15] H. Aboshosha, A. Elshaer, G. T. Bitsuamlak, and A. El Damatty. Consistent inflow turbulence generator for les evaluation of wind-induced responses for tall buildings. *Journal of Wind Engineering and Industrial Aerodynamics*, 142:198–216, 2015.

[16] N. Jarrin, S. Benhamadouche, D. Laurence, and R. Prosser. A synthetic-eddy-method for generating inflow conditions for large-eddy simulations. *International Journal of Heat and Fluid Flow*, 27(4):585–593, 2006.

[17] N. Jarrin. *Synthetic inflow boundary conditions for the numerical simulation of turbulence*. PhD thesis, University of Manchester, 2008.

[18] R. Laraufie, S. Deck, and P. Sagaut. A dynamic forcing method for unsteady turbulent inflow conditions. *Journal of Computational Physics*, 230(23):8647–8663, 2011.

[19] R. Poletto, T. Craft, and A. Revell. A new divergence free synthetic eddy method for the reproduction of inlet flow conditions for les. *Flow, turbulence and combustion*, 91(3):519–539, 2013.

[20] A. Keating, U. Piomelli, E. Balaras, and H.J. Kaltenbach. A priori and a posteriori tests of inflow conditions for large-eddy simulation. *Physics of Fluids*, 16(12):4696–4712, 2004.

[21] N Jarrin, R Prosser, J-C Uribe, S Benhamadouche, and D Laurence. Reconstruction of turbulent fluctuations for hybrid rans/les simulations using a synthetic-eddy method. *International Journal of Heat and Fluid Flow*, 30(3):435–442, 2009.

[22] B. Blocken, T. Stathopoulos, and J. Carmeliet. Cfd simulation of the atmospheric boundary layer: wall function problems. *Atmospheric Environment*, 41:238–252, 2007.

[23] A. Parente, C. Gorle, J. van Beeck, and C. Benocci. A comprehensive modelling approach for the neutral atmospheric boundary layer: consistent inflow conditions, wall function and turbulence model closure. *Boundary Layer Meteorology*, 140(3):411–428, 2011.

[24] L. Amerio. Numerical and experimental analysis of peak pressure loads on rectangular building. 2014.

[25] L. Amerio and A. Zasso. Experimental investigation on the time-space distribution of peak pressure events on high-rise building façades. *Submitted*, 2017.

[26] J. Towns, T. Cockerill, M. Dahan, I. Foster, K. Gaither, A. Grimshaw, V. Hazlewood, S. Lathrop, G. D. Lifka, D.and Peterson, et al. Xsede: accelerating scientific discovery. *Computing in Science & Engineering*, 16(5):62–74, 2014.

[27] PJ Richards and RP Hoxey. Appropriate boundary conditions for computational wind engineering models using the $k-\epsilon$ turbulence model. *Journal of wind engineering and industrial aerodynamics*, 46:145–153, 1993.

[28] Meng Wang and Parviz Moin. Dynamic wall modeling for large-eddy simulation of complex turbulent flows. *Physics of Fluids*, 14(7):2043–2051, 2002.

[29] A Dagnew and Girma T Bitsuamlak. Computational evaluation of wind loads on buildings: a review. *Wind Struct*, 16(6):629–660, 2013.

[30] V. Holmén. Methods for vortex identification. *Master's Theses in Mathematical Sciences*, 2012.

[31] G. I. Taylor. The spectrum of turbulence. In *Proceedings of the Royal Society of London A: Mathematical, Physical and Engineering Sciences*, volume 164, pages 476–490. The Royal Society, 1938.

[32] U. Schumann. Realizability of reynolds-stress turbulence models. *The Physics of Fluids*, 20(5):721–725, 1977.

[33] J. Sousa and G. Paniagua. Entropy minimization design approach of supersonic internal passages. *Entropy*, 17(8):5593–5610, 2015.

[34] M. Caramia and P. Dell' Olmo. Multi-objective optimization. *Multi-objective Management in Freight Logistics: Increasing Capacity, Service Level and Safety with Optimization Algorithms*, pages 11–36, 2008.